Holding Forces of Single-Particle Dielectrophoretic Traps

Joel Voldman,* Rebecca A. Braff,* Mehmet Toner,[†] Martha L. Gray,* and Martin A. Schmidt*

*Massachusetts Institute of Technology, Cambridge, Massachusetts 02139, and [†]Harvard Medical School, Cambridge, Massachusetts 02138 USA

ABSTRACT   We present experimental results and modeling on the efficacy of dielectrophoresis-based single-particle traps. Dielectrophoretic forces, caused by the interaction of nonuniform electric fields with objects, have been used to make planar quadrupole traps that can trap single beads. A simple experimental protocol was then used to measure how well the traps could hold beads against destabilizing fluid flows. These were compared with predictions from modeling and found to be in close agreement, allowing the determination of sub-piconewton forces. This not only validates our ability to model dielectrophoretic forces in these traps but also gives insight into the physical behavior of particles in dielectrophoresis-based traps. Anomalous frequency effects, not explainable by dielectrophoretic forces alone, were also encountered and attributed to electrohydrodynamic flows. Such knowledge can now be used to design traps for cell-based applications.

INTRODUCTION

Dielectrophoretic (DEP) particle traps have been successfully used for many biological applications to date. Such traps operate through the interaction of induced polarization charge with nonuniform electric fields and can induce trapping at either electrode edges (positive DEP) or electric-field intensity minima (negative DEP). The diversity of applications includes particle separation by differential dielectric properties (Gascoyne et al., 1997; Cheng et al., 1998; Markx et al., 1994; Talary et al., 1995), force calibrations of optical tweezers (Fuhr et al., 1998), measurement of bacterial flagellar thrust (Hughes and Morgan, 1999), three-dimensional positive-DEP traps (Suehiro and Pethig, 1998), and extraction of electrical properties or validation of the DEP theory itself (Watarai et al., 1997; Hartley et al., 1999; Jones and Bliss, 1977; Kallio and Jones, 1980). Though applications have used multi-particle traps, in principle, large arrays of traps could be used for the capture and analysis of many individual particles. In these applications it is also likely that fluid will be used to deliver and remove particles (perhaps selectively) from the traps. Ultimately, reaching this potential will require a large array of DEP-based single-particle traps and thus the need for systematic quantitative analysis of their efficacy, which we define as their ability to hold a cell against fluid flow.

To this end we have compared experimental results on the efficacy of a common electrode trap geometry, the planar quadrupole, with predictions from a simulation environment developed to model such traps. We have used beads instead of cells because of their more uniform and well-known physical and electrical properties, which eases comparison with the models. The results have wide signif-icance. First, the synthesis of a complete DEP-based modeling environment, including multi-order DEP forces and exact hydrodynamic (HD) drag force formulations, together with its experimental validation, allows for quantitative design of the efficacy of DEP-based cell traps. In principle, therefore, one can now perform comparative analyses to design DEP traps with differing characteristics for various microscale cell-analysis applications, including single-cell traps for large-array applications. Second, the measurement technique we demonstrate here, again in conjunction with the model, allows us to determine sub-piconewton forces at the microscale. The measurement technique is similar to previous methods of calibrating optical tweezers (Wright et al., 1994; Svoboda and Block, 1994), which have the same fundamental physics as DEP traps. Thus, some applications of optical tweezers where accurate force analyses are needed may be candidates for study using our methods.

THEORY

The dielectrophoretic force in its simplest implementation is the interaction of a nonuniform electric field with the dipole moment it induces in an object. The prototypical case is the induced dipole in a lossy dielectric spherical particle. The force in this case, where the particle is much smaller than the electric field nonuniformities, is given by

$$\mathbf{F}^{(1)} = 2\pi\varepsilon_1 R^3 \mathrm{Re}[\underline{CM}(\omega) \times \nabla\underline{\mathbf{E}}^2(\mathbf{r})], \tag{1}$$

where $\mathbf{F}^{(1)}$ refers to the dipole approximation to the DEP force, ϵ_1 is the permittivity of the medium surrounding the sphere, R is the radius of the particle, ω is the radian frequency of the applied field, $\mathbf{r}$ refers to the spatial coordinate, and $\underline{\mathbf{E}}$ is the complex applied electric field. $\underline{CM}$ is the Clausius-Mossotti (CM) factor, which, for a lossy dielectric uniform sphere (such as a bead), is given by

$$\underline{CM} = \frac{\underline{\varepsilon}_2 - \underline{\varepsilon}_1}{\underline{\varepsilon}_2 + 2\underline{\varepsilon}_1}, \tag{2}$$

where $\underline{\epsilon}_1$ and $\underline{\epsilon}_2$ are the complex permittivities of the medium and the particle, respectively, and are each given by $\underline{\epsilon} = \epsilon + \sigma/(j\omega)$, where ϵ is the permittivity of the medium or particle, σ is the conductivity of the medium or particle, and j is $\sqrt{-1}$.

Eq. 1 shows that the spatial and frequency components of the DEP force are separately contained in the $\nabla\underline{\mathbf{E}}^2$ and $\underline{CM}$ terms, respectively. Depending on the sign of the CM factor, the DEP force propels particles to either the electric field maxima (positive DEP, or p-DEP) or minima (negative DEP, or n-DEP).

Eq. 1 is the simplest approximation to the DEP forces, and although it is applicable in the majority of situations, there will be instances where the field is sufficiently spatially nonuniform (in comparison with the size of the particle) to induce quadrupolar and higher-order moments in the object. In addition, at field nulls the dipole moment, because it is proportional to $\mathbf{E}$, is zero, and thus this dipole approximation to the DEP force will also be zero. In the mid-nineties Washizu and Jones (Jones and Washizu, 1996; Washizu and Jones, 1994, 1996) developed a computationally accessible approach to calculating higher-order DEP forces, which we have implemented into our model (see Appendix). A compact tensor formulation of their result (Jones and Washizu, 1996) is

$$\mathbf{F}^{(n)} = \frac{\overset{\overset{\cdots}{}}{p}^{(n)}[\,\cdot\,]^n(\nabla)^n\mathbf{E}}{n!},\tag{3}$$

where n refers to the force order ($n = 1$ is the dipole, $n = 2$ is the quadrupole, etc.), $\overset{\overset{\cdots}{}}{p}^{(n)}$ is the multipolar induced-moment tensor, and $[\cdot]^n$ and ∇^n represent n dot products and gradient operations. Thus we see that the nth force order is given by the interaction of the nth-order multipolar moment with the nth gradient of the electric field. The multipolar CM factor for a uniform lossy dielectric sphere is given by

$$\underline{CM}^{(n)} = \frac{\underline{\epsilon}_2 - \underline{\epsilon}_1}{n\underline{\epsilon}_2 + (n+1)\underline{\epsilon}_1}.\tag{4}$$

The HD drag force is related to the flow rate in the chamber in a similar manner as Stokes' drag on a sphere in shear flow, with a correction for the effects of the wall (Goldman et al., 1967). The force is given by

$$F_{\text{drag}} = 6\pi\mu R(4V_c/h)F_{\text{drag}}^* z,\tag{5}$$

where μ is the viscosity of the liquid, V_c is the fluid velocity in the middle of the channel, h is the channel height, F_{drag}^* is a nondimensional factor incorporating the wall effects, and z is the height of the center of the sphere. For a parallel plate flow chamber, V_c is linearly related to the volume flow rate.

MATERIALS AND METHODS

Stock solutions

Solutions of two different conductivities, 0.01 S/m and 0.75 mS/m, were made by taking deionized (DI) water with 0.05% Triton X-100 (Sigma, St. Louis, MO) added and adding appropriate amounts of Hanks' balanced salt solution (Gibco BRL, Grand Island, NY), also with 0.05% Triton X-100, until the nominal conductivity was reached, as indicated by an Orion model 125 conductivity meter (Beverly, MA). Solutions were filtered through a 0.45-μm filter (Micron Separations, Westborough, MA), and their conductivity was measured before each use.

Beads

Polystyrene beads (incorporating 2% divinyl benzene), with density 1.062 g/cm^3, in three diameters (7.58 μm (0.08 μm SD), 10.00 μm (0.09 μm SD), and 13.20 μm (0.89 μm SD)) packaged as 10% solids in water were purchased from Bangs Laboratories (Fishers, IN). A 15-μl aliquot of each bead solution was washed twice in 1.5 ml of the appropriate conductivity stock solution and finally resuspended in 1.5 ml of stock solution. All bead solutions were refrigerated and used within 2 months.

Electrode traps

Thin-film quadrupole electrodes were fabricated using conventional microfabrication processes. Standard (25 x 75 mm) microscope slides were cleaned for 10 min in a Piranha solution (3:1 H$_2$SO$_4$:H$_2$O$_2$) and blow dried. Photolithography was then performed using the image-reversal photoresist Hoechst AZ-5214 (Somerville, NJ), which gives re-entrant resist profiles, to define the electrode patterns. Then, 200 Å of chrome and 5000 Å of gold were evaporated onto the slides followed by resist dissolution and metal liftoff in acetone. Finally, the slides were cleaned in methanol and isopropanol and blow dried. A micrograph of the completed electrodes is shown in Fig. 1 *A*, along with relevant dimensions.

Packaging

The packaging scheme is shown in Fig. 1 *B*. Fluid inlet and outlet holes were drilled in the glass slides with 0.75-mm diamond drill bits (C.R. Laurence, Los Angeles, CA). Poly(dimethylsiloxane) gaskets, cast in machined molds from monomer (Sylgard 184, Dow Corning, Midland, MI), above and below the slide functioned as the spacer material and bottom sealing gasket, respectively. The top of the chamber consisted of a glass slide that had been cut to a width of 16 mm and clamped down using an aluminum block. With this setup, the flow chamber sustained >200-μl/min flows without leaking.

Chamber height measurement

The chamber height of the fully assembled unfilled package was measured at various points with an optical interferometer coupled to a z-axis linear gage (543 Series, Mitutoyo/MTI Corp., Aurora, IL) on a Nikon microscope (UM-2, Nikon, Melville, NY). Corrections were made for the indices of refraction of the different materials. The measured chamber height was 0.73 ± 0.01 mm.

Electrical excitation

Sine wave excitation up to 20 MHz and 10 V$_{pp}$ (into 50 Ω) was generated by an HP 3314A signal generator (Hewlett-Packard, Palo Alto, CA). This signal was split and sent into four high-speed amplifiers (LM7171, Analog
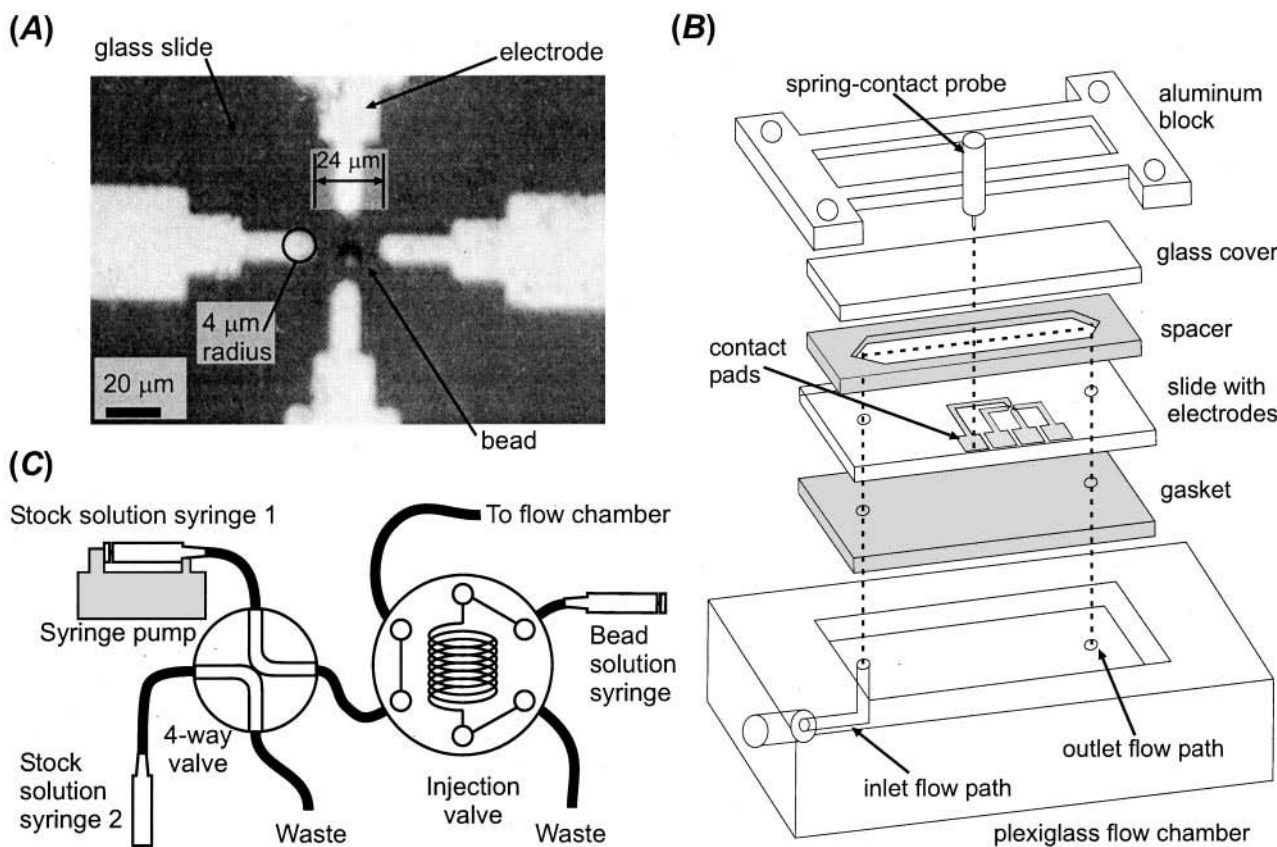
FIGURE 1   (A) Micrograph of the completed quadrupole electrodes, showing a single 10.00-μm bead captured in trap; (B) Schematic of packaging assembly, showing the stack of layers comprising the flow chamber along with the electrical connections via spring-contact probes; (C) Schematic of fluidic subsystem.

Devices, Norwood, MA), 2 noninverting and 2 inverting, that amplified the signal 2$\times$. The amplifiers delivered 180° phase-shifted signals with negligible gain and phase error up to 10 MHz. The output from the amplifiers was sent via coaxial spring-contact probes (Interconnect Devices, Kansas City, KS) to the contact pads at the edge of the glass slide (Fig. 1 B).

Fluidics

Fluidic connection to the package was made via HPLC connectors and tubing (Fig. 1 C). The fluidic test subsystem consisted of a four-way valve (V-101D, Upchurch Scientific, Oak Harbor, WA) that allowed the interchange of syringes without introducing bubbles. The bead solution was injected into the flow using an injection valve (V-450, Upchurch Scientific). Flow was initiated by a syringe pump (KD-101, KD Scientific, Boston, MA) using a 5-ml Hamilton luer-lock syringe (1005TLL, Reno, NV).

Optics

The beads were viewed using a Microzoom microscope (Wentworth Labs, Brookfield, CT) with long-working distance objectives on a semiconductor probe station. Images could be captured using a Panasonic WV-D5000 video camera (Secaucus, NJ) and a Sony VCR.

Release flow rate definition and measurements

Once beads were captured in the quadrupole trap, flow was initiated. In the parallel-plate flow chamber, beads experienced a transverse hydrodynamic force that tended to dislodge them from equilibrium at the center of the trap (Fig. 2). If the bead was held in the trap at the end of 2 min, the bead was considered captured. This time was chosen empirically by observing that beads held for 2 min, if the flow was continued, would usually (>90%) be held indefinitely (tested up to ~5–10 min). The flow rate was adjusted to find the minimum flow rate (within 1 μl/min) at which the bead was released within 2 min. This is termed the release flow rate. The flow rate was adjusted above and below the release flow rate to ensure that the true release flow rate was determined. In practice, one bead could be used repeatedly by stopping the flow after it was just released, in which case it would fall back into the trap.

Modeling

The modeling environment, described more fully in the Appendix, used commercially derived electric-field data (Maxwell 3D, Ansoft, Pittsburgh, PA) and experimental parameters and, using Matlab (R11, The Mathworks, Natick, MA), determined whether the particle would be held in a given flow. It did this by first computing the multipolar DEP, gravitational, and HD drag forces on the particle everywhere in space and then determining whether stable points of zero net force existed. By varying the applied flow rate for a given set of experimental conditions, the modeling environment could determine when the zero-net-force points ceased to exist and thus the release flow rate. For the current work we simulated the upper half of the trap in Fig. 1 A, using symmetry boundary conditions at the glass substrate. Field data from the central portion of the quadrupole was written to a grid, using a grid spacing of 0.5–2 μm, and smoothed using a three-dimensional
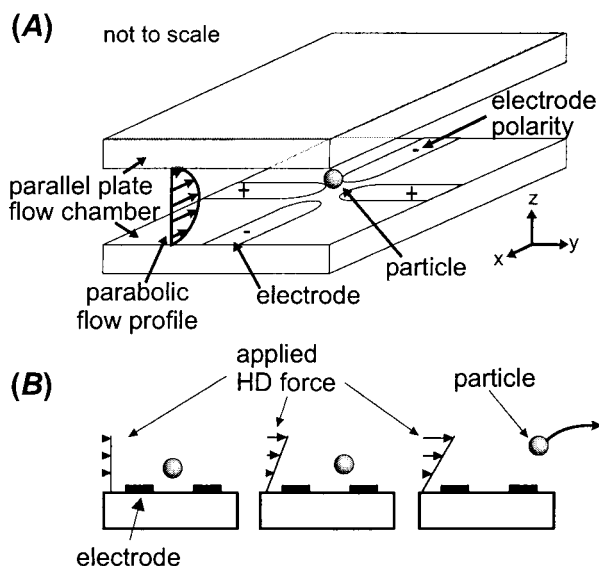
FIGURE 2 (*A*) Schematic of flow chamber, showing a bead in the trap experiencing a parabolic HD drag force; (*B*) Release flow rate and holding force measurements. The flow rate (force) is increased until the bead is liberated from the trap. The parabolic flow profile is approximately linear when the particle is close to the substrate.

Gaussian low-pass filter with the following parameters: three-grid-point convolution kernel (in each direction) with a standard deviation of 1.3 grid points. The filtering was used in lieu of long simulation times to reduce high-spatial-frequency noise.

RESULTS

Single-bead holding

Fig. 1 *A* shows a trap holding a single 10.00-μm bead. Interestingly, even with these unoptimized traps, we have demonstrated single-bead capture: when two beads are captured in a trap, the second bead will be held with much less force than the first, meaning that we can apply a flow rate that will selectively remove the second while still holding the first.

Release flow rate as the voltage is varied: the holding characteristic

If we vary the voltage and measure the release flow rate, we generate the holding characteristic of the trap for a particular set of experimental conditions. By comparing the shape and absolute values of the measured holding characteristic with the predictions based upon the modeling environment, we can evaluate the accuracy and completeness of the modeling environment. The typical shape of the holding characteristic for these traps is shown in Fig. 3 *A* for 7.58-μm beads in 0.01-S/m solutions at a frequency of 1 MHz. The characteristic behavior in these traps is that the release flow rate increases from zero until a maximum
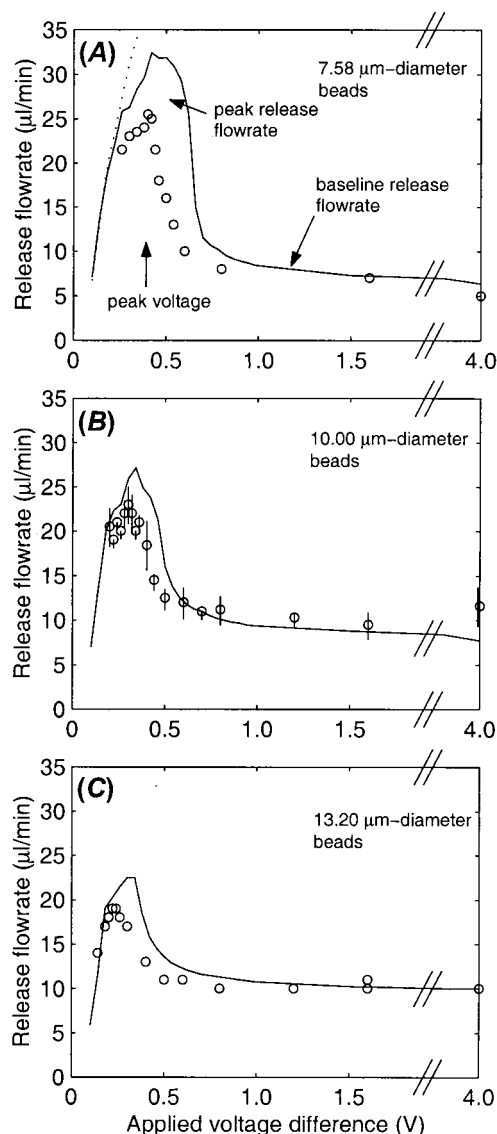
FIGURE 3 Experimental (◯) and simulated (——) holding characteristics for beads in the planar quadrupole trap of Fig. 1 *A* as the bead diameter was varied. Bead diameters were 7.58 μm (*A*), 10.00 μm (*B*), and 13.20 μm (*C*), respectively. Subplot (*B*) shows the long-term scatter in the data, which can be taken as typical of the other curves. Also shown in *A* are the simulated holding characteristics including only dipole DEP force terms (· · ·). The frequency is 1 MHz and the solution conductivity is 0.01 S/m. Note the break in the voltage axis.

release flow rate (the peak release flow rate) is achieved (at the peak voltage), after which it decreases quickly and then reaches a plateau (the baseline release flow rate). To validate our model, we have compared the match between these three parameters, as they define the shape of the holding characteristic.

To get a sense of the scatter in our experimental results, we repeatedly took data for the 10.00-μm beads using more than 10 different beads over 3 months. Individual release

flow rates were measured between one and nine times, with each measurement being double-checked. We have included this scatter and the flow rate discretization error in Fig. 3 *B*. The other data shown in the paper can be assumed to possess similar scatter over this time frame. We then used these results as an internal control when acquiring the rest of the data presented in this paper. We did this by taking data from equivalent conditions during subsequent runs to establish experimental precision. When this was inconvenient (as with different solution conductivities) we used our prior knowledge that the curves should not greatly shift to check against our previous data. In addition, equivalent data points were taken before and after each experimental run to estimate any short-term drift (usually <5%). We did observe a long-term downward drift (toward lower release flow rate) in the release characteristic of ~16% (which therefore accounts for the majority of the scatter). Several factors could account for this trend, such as changes in the chamber geometry, experimental solutions, or room temperature.

Turning back to Fig. 3 *A*, we also show the predicted holding characteristics calculated including either only the dipole ($n = 1$, dotted line) or dipole and quadrupole (solid line) DEP force terms (Eq. 3). One sees that computing only the dipole term gives a monotonically increasing holding characteristic (dotted line) because the *z*-directed force from the dipole term is not strong enough to induce levitation near the field null, where the particle is located. As described below, this levitation is the key to the shape of the holding characteristic. Including the quadrupole term accurately models the problem, because it correctly accounts for the levitation force in quadrupole traps, in agreement with previous work (Washizu et al., 1993; Hartley et al., 1999; Schnelle et al., 1999a). Incorporating the octopole term does not qualitatively or quantitatively change the results, indicating that induced octopoles are negligible in this situation (data not shown).

The match between the experiment and the second-order simulations is significant, especially considering that there are no free parameters. The simulations predict a higher release flow rate (27%) at the peak voltage, a higher peak voltage (5%), and a higher baseline release flow rate (8%).

The trend in release flow rate as the voltage is varied (Fig. 3 *A*) is initially nonintuitive, but becomes apparent when one recognizes that the DEP force influences the height of the particle. This is shown in Fig. 4, where we plot the predicted release flow rate along with the predicted holding force and the predicted height of the particle at release for a 7.58-μm bead in our trap.

When no voltage is applied, there is no confining force, and neglecting any stiction effects between the bead and the surface of the glass slide, which have been measured at less than 1–2 μl/min, the release flow rate should be zero. As the voltage is increased, the DEP forces will create a confining well (Fig. 4 *A*). In this prelevitation regime, the *z*-directed component of this force, which serves to levitate the bead, will initially not be large enough to overcome the gravitational force, and thus the bead will remain on the slide surface. The force pushing the bead from the trap, the fluid flow, varies linearly with height of the bead and volume flow rate (Eq. 5). Thus, if the bead height does not change but the confining forces increase, the release flow rate will also increase.

At some threshold voltage, the *z*-directed DEP force will exactly balance the gravitational force and the bead will start to be levitated (Fig. 4 *B*). This voltage corresponds to the peak voltage and peak flow rate. Any increase past this voltage and the bead will be levitated upwards and then experience larger HD drag forces (Eq. 5). As can be seen from Fig. 4, the height of the particle (dashed line) increases quickly with voltage once it is levitated, and the particle will experience a rapid ascent. Therefore, the increased exposure to the HD drag forces with little increase in the DEP force causes the release flow-rate characteristic to decrease. This can be contrasted with simulations involving only the dipole DEP-force term (Fig. 3 *A*, dotted line) where the release

FIGURE 4 Explanation of holding characteristics as voltage is varied, showing the simulated release flow rate (——), the holding force (— · —), and the height of the particle when it is released (- - -). (*A*) Prelevitation. At very low voltages, the gravitation force cannot overcome the *z*-directed DEP force, and the bead is not levitated. (*B*) Rapid ascent. At a certain voltage the bead will just become levitated and the holding characteristics will peak. (*C*) Saturation. At high voltages, the increase in holding force is balanced by the increased particle levitation height, resulting in a flat release flow-rate profile.
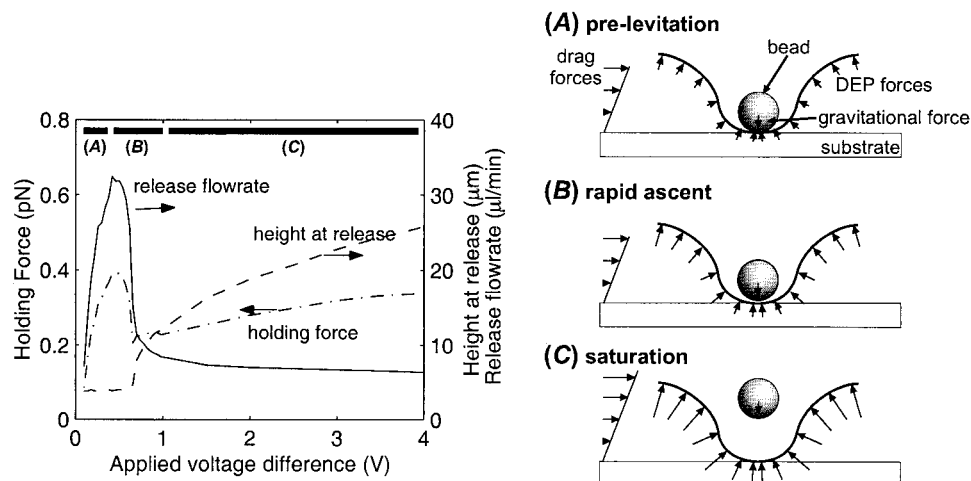
flow rate never decreases because the particle never becomes levitated.

Observing the particle height versus voltage curve (Fig. 4, dashed line), one sees that after an initial rapid ascent, the slope of the curve decreases and saturates because the z-directed DEP forces decrease rapidly as the bead is levitated away from the electrodes. This is in accord with the measured height-versus-voltage characteristics of other researchers (Fuhr et al., 1992a). At this point, the holding force increases with voltage (Fig. 4, dash-dotted line) are matched by the increases in the HD drag forces due to the increased particle height (Fig. 4, dashed line and Eq. 5). They thus balance each other and give a saturated flat release-flow rate characteristic (Fig. 4C, solid line).

Holding characteristic as the particle diameter is varied

Since the DEP forces vary as R^3 (dipole) and R^5 (quadrupole), the gravitational force varies with R^3, and the HD drag forces vary with R, we can use differing particle sizes to evaluate the accuracy of our modeling environment to see whether it predicts the correct particle size effects. This will help us determine whether we are modeling these forces adequately and whether other forces are significant. We have performed experiments with three different bead sizes to explore this trend. The results are shown in Fig. 3, along with the predicted results (simulated including up to the $n = 2$ DEP force term). Although all three bead diameters show the same characteristic peaking-declining-plateau response, the values of the peak release flow rate, peak voltage, and baseline release flow rates all differ as the bead diameter changes.

These differences are shown Fig. 5, where the three parameters that define the holding characteristic have been extracted from the simulation and experimental results. In making this comparison we extracted parameters from only one data set consisting of three runs at different bead diameters to eliminate the long-term drift seen in Fig. 3 B (and thus we use only a subset of the data displayed in Fig. 3 B). The scatter was estimated from the uncertainty in the peak height ($n = 7$ data points for 10.00-μm beads; $n = 2$ for other diameters) and position ($n = 5$ for 10.00-μm beads; $n = 2$ for others) during these runs and from the release flow rates collected at voltages greater than 0.8 V for the baseline ($n \geq 6$ for each diameter). In all cases, the scatter was <17% and usually was <5%.

We see that as the bead diameter is increased, the baseline release flow rate (Fig. 5 C) increases whereas both the peak voltage (Fig. 5 A) and peak release flow rate (Fig. 5 B) decrease. The absolute agreement between simulations and experiment is quite good, with the dependencies captured quantitatively; the maximum differences are 30% for the peak voltage, 27% for the peak flow rate, and 9% for the baseline release flow rate.
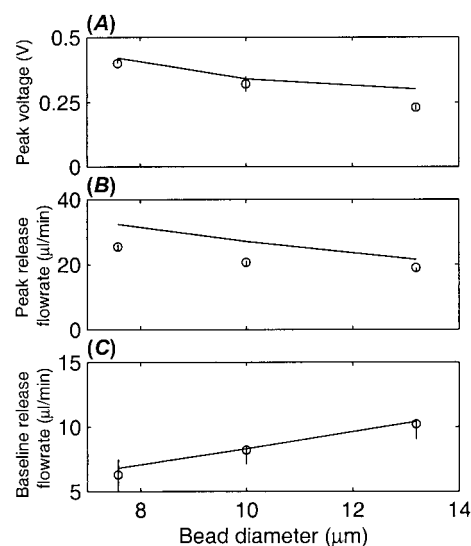
FIGURE 5 Comparison of extracted experimental ($\bigcirc$) and simulated (——) peak voltage (A), peak release flow rate (B), and baseline release flow rate (C) from one data set. The frequency is 1 MHz and the solution conductivity is 0.01 S/m.

The trends (Fig. 5) can be explained in accordance with DEP theory. As the bead diameter is increased, the voltage necessary to initially levitate the bead (which corresponds to the peak voltage) will decrease because the levitation forces increase with bead diameter. These smaller voltages cause the bead to experience smaller DEP confining forces before being levitated. This leads to the decrease in peak release flow rate with bead diameter. Finally, the increasing baseline release flow rate with diameter is due to the fact that whereas the HD drag forces increase only linearly with diameter, the DEP confining forces increase as R^3 and R^5.

Holding characteristic changes with frequency

Whereas the first two trends (voltage and bead diameter) evaluate the spatial aspects of our model, the frequency trends are a test of the CM factor of the DEP force, which is the only frequency-dependent component that we have included. The CM factor (Eq. 2) for 10.00-μm-diameter beads is shown in Fig. 6. Although only the dipole term of the CM factor is shown, the quadrupole and higher terms display similar behavior, although at slightly different dispersion frequencies and smaller ranges (e.g., the quadrupole term can only vary between $-1/3$ and $+1/2$). To generate Fig. 6, the conductivity of the beads was estimated by using very-low-conductivity stock solutions and measuring the n-DEP to p-DEP transition frequencies, when the beads would switch from being repelled from to being attracted to the electrodes, respectively. Fitting these to the zeros of the CM factor gave a conductivity estimate of $2e^{-4}$ S/m, which
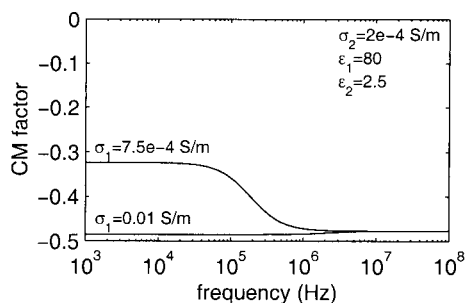
FIGURE 6 Calculated CM factor (dipole term) for a polystyrene bead in salt solution.

is in accord with literature values for unmodified polystyrene beads of this size (Arnold et al., 1987).

As the frequency is decreased, the CM factor goes from being permittivity dominated to conductivity dominated.

For the high-conductivity solution (0.01 S/m), no dispersion is apparent because the CM factor is dominated by the properties of the stock solution. For the low-conductivity solution (0.75 mS/m), the CM factor decreases in magnitude as the frequency is decreased. Because the CM factor directly multiplies the DEP force equation (Eq. 1), changes in the CM factor will cause corresponding changes in the DEP force at a given voltage. Thus, we expect little frequency dependence of the forces at 0.01 S/m and some dependence at 0.75 mS/m. In essence, the CM factor changes are equivalent to scaling along the voltage axis and should thus shift the holding characteristic only along that dimension.

Two frequency sweeps were performed, at both high (0.01 S/m) and low (0.75 mS/m) solution conductivities. Both of the 1-MHz holding characteristics (Fig. 7, *A* and *D*) agree well with predictions, although the peak flow rates and peak voltages are smaller than predicted. Although these predictions can be partly explained by the sensitivity
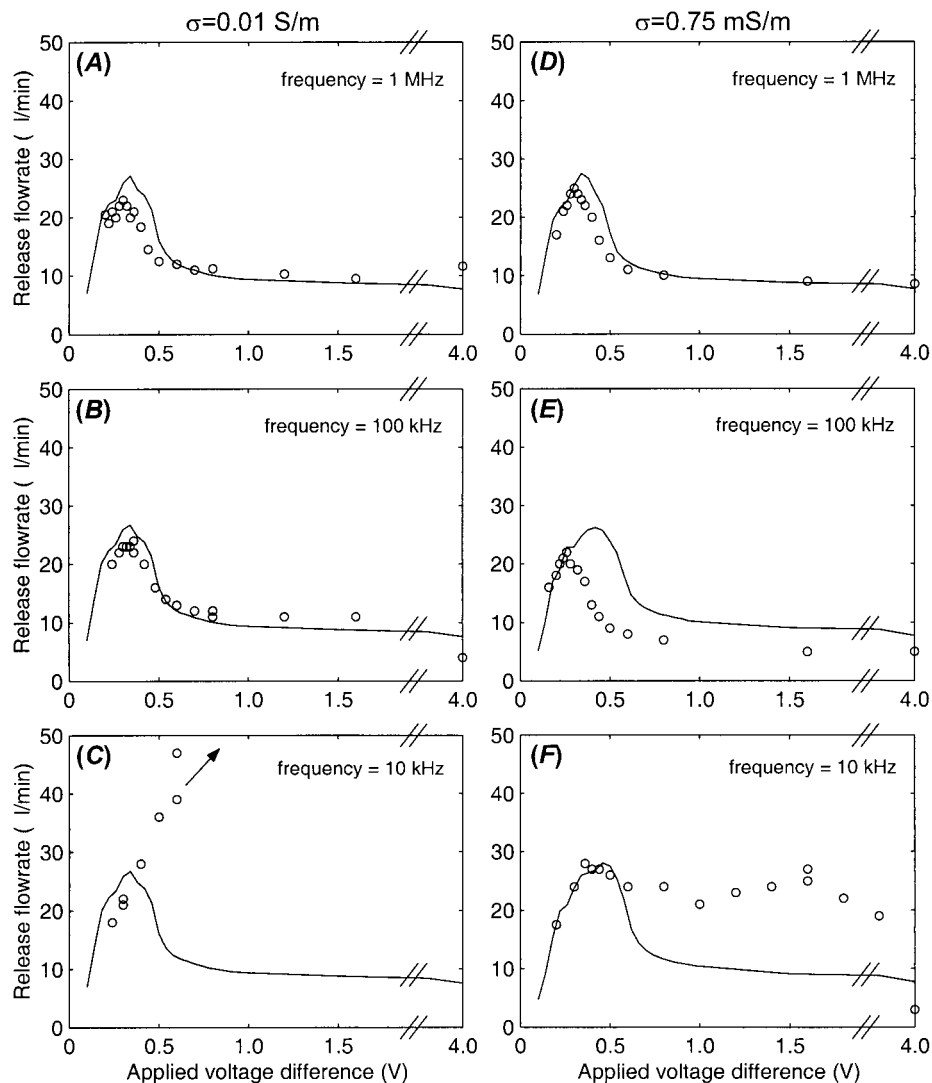
FIGURE 7 Experimental (○) and simulated (——) holding characteristics for 10.00-μm beads for three different frequencies at solution conductivities of 0.01 S/m (*A–C*) and 0.75 mS/m (*D–F*). Results are shown for frequencies of 1 MHz (*A* and *D*), 100 kHZ (*B* and *E*), and 10 kHz (*C* and *F*). The 10-kHz holding characteristic at 0.01 S/m (*C*) increases quickly with voltage and so is truncated in the plot. Note the break in the voltage axis.

of the simulations around the peak flow rate, they could also be due to temperature changes in the measurement room, causing the chamber height and experimental properties to change, or experimental observations of neglected forces. The 100-kHz holding characteristics (Fig. 7, *B* and *E*) for both solutions also have the predicted shape, although the low-conductivity characteristic (Fig. 7 *E*) deviates more from predictions than the 0.01 S/m characteristic (Fig. 7 *B)*. The 10-kHz holding characteristics (Fig. 7, *C* and *F*) for both solution conductivities exhibit very different shapes that cannot be explained by our modeling environment.

The only frequency dependence included in our modeling environment is through the CM factor. The 10-kHz curves, which show completely different holding characteristics, can clearly not be explained through manipulation of the CM factor. The 100-kHz curve at the low-conductivity solution has the same characteristic shape but is shifted toward lower voltages and release flow rates. As explained before, the release flow-rate shift cannot be caused by changes in the CM factor. For the voltage shift to be caused by changes in the CM factor, the CM factor would have to decrease (become more negative) at low frequencies. Not only would this require an extremely small (and physically dubious) bead conductivity ($\sim 1e^{-6}$ S/m), but because the CM factor is already near its theoretical minimum, the increase in the magnitude of the CM factor would be much too small to account for the experimental observations (data not shown).

The shifts in the 100-kHz (and also possibly the 1-MHz) holding characteristics can be more readily explained by the existence of an upward destabilizing force on the bead. The 10-kHz characteristics are consistent with the existence of an extra confining force on the bead. Thus, we conclude that the cause of the discrepancies is due to other forces that are not accounted for in our model, as discussed below.

DISCUSSION

We have demonstrated the ability to trap and hold single particles with holding characteristics predicted by a model. These holding characteristics correspond to forces in the sub-piconewton range, which is a biophysically relevant force regime. In addition, we have predicted trends as both the voltage and bead radius are varied, alluding to the likely generalizability of the modeling environment. Frequency effects are not predicted accurately, probably (as discussed below) because forces present at lower frequencies were not accounted for.

DEP force measurements

The development of the multipolar DEP theory coupled with the decreasing cost of computing power and the increasing sophistication of microscale DEP researchers has led to several recent attempts to construct quantitative DEP microdevices that are amenable to modeling. Recent work (Schnelle et al., 1999b; Muller et al., 1999) has even started to concentrate on the interaction between DEP and HD forces, in their case determining the flow needed to break through a DEP barrier, similar to our case. The difference between their situation and the one presented here is that the particles in that work are located at the centerline of Poiseuille flow, and thus the drag force is well defined by the Stokes drag on a sphere. This allows them to derive analytical representations for the force balance. As particles approach surfaces, this analytical formulation becomes hopelessly complicated, necessitating a numerical approach, as we have taken.

Our experimental approach, the determination of release flow rate, has many advantages over direct measurements of the DEP force. First, the efficacy of particle traps in many applications will be the ability of the trap to hold a particle against fluid flow. Thus, this measurement, even if not correlated to theory, would still be valuable. The comparison with theory, however, is ultimately more useful, because the validation of the modeling environment allows for future trap design with confidence that the fundamental physics in a specific operating regime of interest are being accounted for.

There are several implications of these results for such future trap design. First, larger voltages are not necessarily better; optimal holding occurs in our structures at ~ 0.3 V. The best trapping occurs when particles are deep in a potential energy well. For these planar quadrupole traps, this occurs when the particles are on the substrate or just barely levitated. Second, planar quadrupoles are quite weak traps (holding at <20 μl/min), and so exploring alternate geometries may lead to much higher holding forces. Although operating at low frequencies is one route to higher holding (Fig. 7, *C* and *F*), this regime most likely involves forces other than those accounted for in the model, complicating such designs. If these forces could be understood and harnessed, however, they might themselves provide routes to higher holding.

The agreement with predictions also allows us to extract DEP forces, which themselves are useful for testing the DEP theory itself or determining the electrical properties of particles. Other researchers testing the theory have used particle levitation (Kaler and Jones, 1990; Hartley et al., 1999), flow-induced particle displacement in DEP traps (Fuhr et al., 1998; Muller et al., 1999), and particle velocity measurements in DEP force fields (Cruz and Garcia-Diego, 1997). The release flow rate method described represents a new addition to this list. The close coupling with our numerical modeling environment removes limits that other methods may have with respect to electrode geometries or experimental conditions.

Finally, examining Fig. 4, we see that we are actually determining forces in the sub-piconewton range. This gives

an indication to the sensitivity of our measurement methodology. This is comparable to the force sensitivities of optical tweezers (Wright et al., 1994; Svoboda and Block, 1994), which is the most closely related biophysical measurement. The agreement in shape and actual value of the predicted and measured holding characteristics gives strong validation that we are accounting correctly for the DEP, HD drag, and gravitational forces in our system.

Shear flow approximation to Poiseuille flow

We have used shear-flow drag forces instead of Poiseuille flow (which actually exists within the parallel-plate flow chamber) to compare predictions with experiments. At the bead heights encountered in our experiments, the deviation between the shear and parabolic flow profiles is less than 2%, and thus both models should be expected to give the same drag force and thus holding characteristic. We checked this assumption by comparing predictions using analytically solved drag forces for each flow profile (Ganatos et al., 1980; Goldman et al., 1967). The two drag force formulations gave release flow rates that differed by 10%, which was found to be due to a 10% difference in drag forces predicted by the two theories near the substrate. The reason for the differences is not entirely clear, but we have chosen to use the shear flow model for the following reasons: 1) it involves interpolating within a one-dimensional parameter space, versus two-dimensional for the Poiseuille flow; 2) our regions of operation are well within its parameter space, whereas we are at the asymptotes of the Poiseuille flow model; and 3) it predicts release flow rates that agree better with experiments. Regardless of the flow profile chosen, the predictions are affected by only 10%.

Agreement between predictions and experiments

The absolute agreement between predictions and experiments in Figs. 3 and 5 is remarkable, especially since no fitting parameters were used. This leads us to conclude that we are accurately accounting for the DEP, gravitational, and HD drag forces in our model. One possible cause of the existing discrepancies that we can rule out would be errors associated with physical and experimental parameters such as bead radius and chamber width. Using the modeling environment to perform sensitivity analyses shows that reasonable errors in these quantities would not result in the observed deviations between prediction and experiment.

Other causes of error include the sensitivity of the release flow rate determination around the peak height due to noise in the numerics, Brownian motion of the particle into lower force-confining regions (Hughes, 1998), and electrohydrodynamic (EHD) flows, as discussed below. In addition, although the symmetry of the ideal quadrupole electrode structure precludes any substrate-liquid material interface or charge relaxation effects from affecting the electric fields, the actual physical situation could have asymmetries that cause these effects to appear. A final source of error is that heat generation will cause inhomogeneities in the electrical properties of the system, which could alter the electric fields.

To remove this final source of error and to include the interfacial effects properly in nonsymmetrical electrode geometries, the electric field would need to be calculated self-consistently, including frequency and temperature effects, as others have done (Schnelle et al., 1999b). Here we see the benefit of the arbitrary choice of field solver, as it allows us to easily implement such a change.

Forces responsible for anomalous frequency effects

The experimental results agree with predictions at high frequencies, but as the frequency is lowered, anomalies surface that cannot be explained by manipulating our models. The source of the discrepancies most consistent with observations is forces unaccounted for in our models, which we conclude are induced by EHD flows. We ruled out flow-induced lift forces and linear polarization effects; calculated flow-induced lift forces for our experimental situation are much too small ($\sim 10^{-17}$ N) (Krishnan and Leighton, 1995), and linear polarization effects, which would reducing the electric field in the medium (Schwan, 1992), would affect predictions much as the CM factor does and thus shift the curves only toward higher voltages.

EHD flows, induced by the interaction between either thermally generated or double-layer charge with electric fields in fluids (Ramos et al., 1998; Melcher and Taylor, 1969; Melcher, 1981), can impart either confining or destabilizing forces. The type of force is dictated by the origin of the charge (thermal or double-layer) and the applied frequency relative to the relaxation frequency of the medium (which has the form σ/ϵ) (Ramos et al., 1998, 1999).

Several lines of evidence are consistent with EHD flows being the cause of the release flow rate deviations. First, flows not predicted by DEP theory alone (and attributed to EHD phenomena) have been observed repeatedly by DEP researchers working on microscale electrodes (Fuhr et al., 1992b; Ramos et al., 1998, 1999; Muller et al., 1996; Green and Morgan, 1998). Second, small debris (micron sized) inadvertently introduced into our chamber will flow in circulatory patterns (reminiscent of other reported EHD flow patterns) around the electrodes at various voltages and frequencies. Third, the observed increases (Fig. 7, C and F) and decreases in the holding forces (Fig. 7 E) with frequency are consistent with frequency-dependent changes in the magnitude and direction of the EHD flows (for systems such as ours that possess both thermally induced and double-layer charge). Future work will investigate the nature of the effects for possible incorporation into the modeling environment and additional use as trap effectors on their own.

Thus, based on both our experimental observations and a plausible rationale for frequency-related deviations between model and experiment, we conclude that the modeling environment accounts for DEP, HD drag, and gravitational forces and thus is valid under conditions where other forces are negligible. Avoiding possible EHD effects necessitates design at relatively high frequencies or for relatively large particles. For the applications that we are interested in, involving cells, this regime provides a great deal of latitude in design as we would normally like to operate at high frequencies to minimize induced transmembrane potentials.

CONCLUSIONS

We have used a microfabricated planar quadrupole as a test bed for evaluating DEP-based traps, using polystyrene beads as a model for cells. Using this simple geometry, we have been able to determine fundamental information, such as the trap efficacy. In addition, we have determined HD and DEP forces at the sub-piconewton level. In conjunction with a modeling environment that we have developed, we have been able to compare the predicted and experimental results and found them to be quite close, with no adjusted parameters. Anomalous frequency-dependent behaviors were observed, most likely caused by electrohydrodynamic flows, and do not affect the validity of the modeling environment, but rather provide bounds on the design space where the environment is valid. The combination of modeling and experiments has given us insight into the nature of DEP traps and guides us in the design of stronger single-particle traps for various biological applications.

APPENDIX: MODELING ENVIRONMENT

Electric field calculation

The modeling environment takes as its input electric fields computed via any other method and interpolated onto a regular grid. Simulations can be run using one set of potentials and extrapolated to other voltages by scaling the electric field, using the linearity of the electric field with voltage.

DEP force calculation

The program calculates the full multipolar DEP force using the induced-multipole theory shown in Eqs. 3 and 4. The CM factor is calculated using the solutions for either a solid dielectric sphere (Eq. 4), to model plastic beads, or a dielectric shell, to model cells, using expressions from the literature (Jones, 1995). More complex models could be implemented.

The program uses an innovative iterative force calculation algorithm, which makes it easy to calculate arbitrary DEP force orders. The algorithm requires that we catalog the multiple derivatives of the electric field, which are evaluated using nested loops. We do this with six-dimensional matrices for the electric field and its derivatives arranged as $E(x,y,z,p,q,r)$ where p, q, and r correlate to the number of derivatives of the electric field taken in the x, y, and z directions, respectively. Because Matlab allows only non-

zero addressing into matrices, the following scheme is used:

$$
\begin{aligned}
E(x, y, z, 2, 1, 1) &= E_x \\
E(x, y, z, 1, 2, 1) &= E_y \\
E(x, y, z, 2, 2, 1) &= \frac{\partial E_x}{\partial y} = \frac{\partial E_y}{\partial x} \\
E(x, y, z, 3, 1, 2) &= \frac{\partial^2 E_x}{\partial x \partial z} = \frac{\partial^2 E_z}{\partial x^2} \\
&\vdots
\end{aligned}
\tag{6}
$$

This labeling scheme simplifies the DEP force calculation algorithm, which is given by

$$
F_0^{(n)} = \frac{2}{(n-1)!(2n-1)!!} \pi \varepsilon_1 R^{2n+1} \mathrm{Re}[\underline{CM}^{(n)}]
$$

$$
\langle F_1^{(i)} \rangle, \langle F_2^{(i)} \rangle, \langle F_3^{(i)} \rangle = 0
$$

for $i = 1$ to n; for $p = 0$ to n; for $q = 0$ to $(i - p)$;

$$
r = i - (p + q)
\tag{7}
$$

$$
\langle F_1^{(i)} \rangle = \langle F_1^{(i)} \rangle + F_0^{(i)} E(x, y, z, p+1, q+1, r+1)
$$
$$
\times E(x, y, z, p+2, q+1, r+1)
$$

$$
\langle F_2^{(i)} \rangle = \langle F_2^{(i)} \rangle + F_0^{(i)} E(x, y, z, p+1, q+1, r+1)
$$
$$
\times E(x, y, z, p+1, q+2, r+1)
$$

$$
\langle F_3^{(i)} \rangle = \langle F_3^{(i)} \rangle + F_0^{(i)} E(x, y, z, p+1, q+1, r+1)
$$
$$
\times E(x, y, z, p+1, q+1, r+2)
$$

end; end; end,

where $F_0^{(n)}$ is a constant calculated once. For our situation, the electric fields are real and so we do not need to worry about complex values except for the CM factor.

Other forces

The modeling environment includes three other forces: the gravitational force, the hydrodynamic (HD) drag force on the particle, and a rigid substrate bottom boundary. The magnitude of the gravitational force is given by

$$
F_{grav} = \frac{4}{3} \pi R^3 (\rho_2 - \rho_1) g,
\tag{8}
$$

where ρ_1 and ρ_2 refer to the densities of the medium and the particle, respectively, and g is the gravitational acceleration constant. The HD drag force is calculated using Eq. 6. Our final "force" is the implementation of a rigid bottom boundary defined by the substrate. This allows us to simulate particles sitting on the substrate surface. To do this we automatically adjust the z-directed total force on the particle so that it is zero (or positive) when the particle is sitting on the substrate.

Holding point determination

From the computed forces we can determine whether the trap in this circumstance can indeed hold a particle by finding points in space (called holding points) where the particle experiences zero net force. These are the only points where we can expect to find a particle (at steady state). If we then increase the destabilizing fluid forces and determine when the holding points cease to exist, we can compute the strength of the trap and the release flow rate.

The algorithm proceeds as follows. For each of the three total-force components (F_x, F_y, and F_z) we find the surface where that force component is zero, i.e., the zero-force isosurface. This surface is represented in Matlab using a set of three-to-six-sided polygons. Isosurfaces are calculated using code (Bengtsson, 1997) based on the Marching Cubes algorithm. Once we have the three isosurfaces, we find where they intersect by checking for three-way intersections among the polygons comprising the surfaces. We first do a quick check using a three-dimensional bounding box algorithm (Bourke, 1987) and then perform computations on this set of intermediate polygons to determine whether any three-way intersection points actually exist.

Points found in this way would be holding points if they represented stable force minima. To check this, we implement an algorithm that determines whether $\mathbf{F} \times d\mathbf{r} < 0$ for each direction away from a putative holding point (Blake, 1985). Other more heuristic methods such as volume exclusion are also used.

Finally, by varying the flow rate in the model to find the threshold where no holding points exist we can determine the release flow rate or the holding force.

REFERENCES

Arnold, W. M., H. P. Schwan, and U. Zimmermann. 1987. Surface conductance and other properties of latex particles measured by electrorotation. *J. Phys. Chem.* 91:5093- 5098.

Bengtsson, L. 1997. Equisurf: Isosurface package for Matlab version 5.0. ftp.mathworks.com/pub/contrib/v5/graphics/equisurf/.

Blake, A. 1985. Handbook of Mechanics, Materials, and Structures. Wiley, New York.

Bourke, P. 1987. Determining whether or not a point lies on the interior of a polygon. http://www.mhri.edu.au/~pdb/geometry/insidepoly.

Cheng, J., E. L. Sheldon, L. Wu, A. Uribe, L. O. Gerrue, J. Carrino, M. J. Heller, and J. P. O'Connell. 1998. Preparation and hybridization analysis of DNA/RNA from *E. coli* on microfabricated bioelectronic chips. *Nat. Biotechnol.* 16:541–546.

Cruz, J. M., and F. J. Garcia-Diego. 1997. Dielectrophoretic force measurements in yeast cells by the Stokes method. *In* IAS '97. Conference Record of the 1997 IEEE Industry Applications Conference 32nd IAS Annual Meeting. IEEE, New York, NY. 2012–2018.

Fuhr, G., W. M. Arnold, R. Hagedorn, T. Muller, W. Benecke, B. Wagner, and U. Zimmermann. 1992a. Levitation, holding, and rotation of cells within traps made by high-frequency fields. *Biochim. Biophys. Acta.* 1108:215–223.

Fuhr, G., R. Hagedorn, T. Muller, W. Benecke, and B. Wagner. 1992b. Microfabricated electrohydrodynamic (EHD) pumps for liquids of higher conductivity. *J. Microelectromech. Systems.* 1:141–146.

Fuhr, G., T. Schnelle, T. Muller, H. Hitzler, S. Monajembashi, and K. O. Greulich. 1998. Force measurements of optical tweezers in electro-optical cages. *Appl. Phys. A Mater. Sci. Process.* 67:385–390.

Ganatos, P., R. Pfeffer, and S. Weinbaum. 1980. A strong interaction theory for the creeping motion of a sphere between plane parallel boundaries. II. Parallel motion. *J. Fluid Mech.* 99:755–783.

Gascoyne, P. R. C., X.-B. Wang, Y. Huang, and F. F. Becker. 1997. Dielectrophoretic separation of cancer cells from blood. *IEEE Trans. Ind. Appl.* 33:670–678.

Goldman, A. J., R. G. Cox, and H. Brenner. 1967. Slow viscous motion of a sphere parallel to a plane wall. II. Couette flow. *Chem. Eng. Sci.* 22:653–660.

Green, N. G., and H. Morgan. 1998. Separation of submicrometre particles using a combination of dielectrophoretic and electrohydrodynamic forces. *J. Phys. D Appl. Phys.* 31:L25–L30.

Hartley, L. F., K. Kaler, and R. Paul. 1999. Quadrupole levitation of microscopic dielectric particles. *J. Electrostat.* 46:233–246.

Hughes, M. P., and H. Morgan. 1998. Dielectrophoretic trapping of single submicrometre scale bioparticles. *J. Phys. D Appl. Phys.* 31:2205–2210.

Hughes, M. P., and H. Morgan. 1999. Measurement of bacterial flagellar thrust by negative dielectrophoresis. *Biotechnol. Prog.* 15:245–249.

Jones, T. B. 1995. Electromechanics of Particles. Cambridge University Press, Cambridge.

Jones, T. B., and G. W. Bliss. 1977. Bubble dielectrophoresis. *J. Appl. Phys.* 48:1412–1417.

Jones, T. B., and M. Washizu. 1996. Multipolar dielectrophoretic and electrorotation theory. *J. Electrostat.* 37:121–134.

Kaler, K. V. I. S., and T. B. Jones. 1990. Dielectrophoretic spectra of single cells determined by feedback-controlled levitation. *Biophys. J.* 57:173–82.

Kallio, G. A., and T. B. Jones. 1980. Dielectric constant measurements using dielectrophoretic levitation. *IEEE Trans. Ind. Appl.* 16:69–75.

Krishnan, G. P., and D. T. Leighton. 1995. Inertial lift on a moving sphere in contact with a plane wall in a shear-flow. *Phys. Fluids.* 7:2538–2545.

Markx, G. H., M. S. Talary, and R. Pethig. 1994. Separation of viable and non-viable yeast using dielectrophoresis. *J. Biotechnol.* 32:29–37.

Melcher, J. R. 1981. Continuum Electromechanics. MIT Press, Cambridge, MA.

Melcher, J. R., and G. I. Taylor. 1969. Electrohydrodynamics: a review of the role of interfacial shear stresses. *Annu. Rev. Fluid Mech.* 1:111–146.

Muller, T., A. Gerardino, T. Schnelle, S. G. Shirley, F. Bordoni, G. De Gasperis, R. Leoni, and G. Fuhr. 1996. Trapping of micrometre and sub-micrometre particles by high- frequency electric fields and hydrodynamic forces. *J. Phys. D Appl. Phys.* 29:340–349.

Muller, T., G. Gradl, S. Howitz, S. Shirley, T. Schnelle, and G. Fuhr. 1999. A 3-D microelectrode system for handling and caging single cells and particles. *Biosensors Bioelectron.* 14:247–256.

Ramos, A., H. Morgan, N. G. Green, and A. Castellanos. 1998. Ac electrokinetics: a review of forces in microelectrode structures. *J. Phys. D Appl. Phys.* 31:2338–2353.

Ramos, A., H. Morgan, N. G. Green, and A. Castellanos. 1999. The role of electrohydrodynamic forces in the dielectrophoretic manipulation and separation of particles. *J. Electrostat.* 47:71–81.

Schnelle, T., T. Muller, and G. Fuhr. 1999a. The influence of higher moments on particle behavior in dielectrophoretic field cages. *J. Electrostat.* 46:13.

Schnelle, T., T. Muller, G. Gradl, S. G. Shirley, and G. Fuhr. 1999b. Paired microelectrode system: dielectrophoretic particle sorting and force calibration. *J. Electrostat.* 47:121–132.

Schwan, H. P. 1992. Linear and nonlinear electrode polarization and biological materials. *Ann. Biomed. Eng.* 20:269–288.

Suehiro, J., and R. Pethig. 1998. The dielectrophoretic movement and positioning of a biological cell using a three-dimensional grid electrode system. *J. Phys. D Appl. Phys.* 31:3298–3305.

Svoboda, K., and S. M. Block. 1994. Biological applications of optical forces. *Annu. Rev. Biophys. Biomol. Struct.* 23:247–285.

Talary, M. S., K. I. Mills, T. Hoy, A. K. Burnett, and R. Pethig. 1995. Dielectrophoretic separation and enrichment of CD34$^+$ cell subpopulation from bone marrow and peripheral blood stem cells. *Med. Biol. Eng. Comput.* 33:235–237.

Washizu, M., and T. B. Jones. 1994. Multipolar dielectrophoretic force calculation. *J. Electrostat.* 33:187–198.

Washizu, M., and T. B. Jones. 1996. Generalized multipolar dielectro-phoretic force and electrorotational torque calculation. *J. Electrostat.* 38:199–211.

Washizu, M., T. B. Jones, and K. V. I. S. Kaler. 1993. Higher-order dielectrophoretic effects: levitation at a field null. *Biochim. Biophys. Acta.* 1158:40–46.

Watarai, H., T. Sakamoto, and S. Tsukahara. 1997. In situ measurement of dielectrophoretic mobility of single polystyrene microparticles. *Langmuir.* 13:2417–2420.

Wright, W. H., G. J. Sonek, and M. W. Berns. 1994. Parametric study of the forces on microspheres held by optical tweezers. *Appl. Optics.* 33:1735–1748.